NuSTAR Observations of the State Transition of Millisecond Pulsar Binary PSR J1023+0038

Tendulkar, Shriharsh P.; Yang, Chengwei; An, Hongjun; Kaspi, Victoria M.; Archibald, Anne M.; Bassa, Cees; Bellm, Eric; Bogdanov, Slavko; Harrison, Fiona A.; Hessels, Jason W. T.

Total number of authors:
22

Published in:
Astrophysical Journal

Link to article, DOI:
10.1088/0004-637X/791/2/77

Publication date:
2014

Document Version
Publisher's PDF, also known as Version of record

The Astrophysical Journal, 791:77 (12pp), 2014 August 20 doi:10.1088/0004-637X/791/2/77

NuSTAR OBSERVATIONS OF THE STATE TRANSITION OF MILLISECOND PULSAR BINARY PSR J1023+0038

Shriharsh P. Tendulkar[1], Chengwei Yang[2,3], Hongjun An[2], Victoria M. Kaspi[2], Anne M. Archibald[4], Cees Bassa[4], Eric Bellm[1], Slavko Bogdanov[5], Fiona A. Harrison[1], Jason W. T. Hessels[4,6], Gemma H. Janssen[4], Andrew G. Lyne[7], Alessandro Patruno[8,4], Benjamin Stappers[7], Daniel Stern[9], John A. Tomsick[10], Steven E. Boggs[10], Deepto Chakrabarty[11], Finn E. Christensen[12], William W. Craig[10,13], Charles A. Hailey[5], and William Zhang[14]
[1] California Institute of Technology, 1200 E California Blvd, MC 249-17, Pasadena, CA 91125, USA; spt@astro.caltech.edu
[2] Department of Physics, McGill University, 3600 University St, Montreal, QC H3A 2T8, Canada
[3] National Space Science Center, Chinese Academy of Sciences, 1 Nanertiao, Zhongguancun, Beijing 100190,China
[4] ASTRON, The Netherlands Institute for Radio Astronomy, Postbus 2, 7990 AA, Dwingeloo, The Netherlands
[5] Columbia Astrophysics Laboratory, Columbia University, 550 West 120th Street, New York, NY 10027, USA
[6] Astronomical Institute "Anton Pannekoek", University of Amsterdam, Postbus 94249, 1090 GE Amsterdam, The Netherlands
[7] Jodrell Bank Centre for Astrophysics, School of Physics and Astronomy, The University of Manchester, Manchester M13 9PL, UK
[8] Leiden Observatory, Leiden University, P.O. Box 9513, NL-2300 RA Leiden, The Netherlands
[9] Jet Propulsion Laboratory, California Institute of Technology, Pasadena, CA 91109, USA
[10] Space Sciences Laboratory, University of California, Berkeley, CA 94720, USA
[11] Kavli Institute for Astrophysics and Space Research, Massachusetts Institute of Technology, 70 Vassar Street, Cambridge, MA 02139, USA
[12] DTU Space, National Space Institute, Technical University of Denmark, Elektrovej 327, DK-2800 Lyngby, Denmark
[13] Lawrence Livermore National Laboratory, Livermore, CA 94550, USA
[14] NASA Goddard Space Flight Center, Astrophysics Science Division, Code 662, Greenbelt, MD 20771, USA
Received 2014 February 18; accepted 2014 June 25; published 2014 July 29

ABSTRACT

We report *NuSTAR* observations of the millisecond pulsar–low-mass X-ray binary (LMXB) transition system PSR J1023+0038 from 2013 June and October, before and after the formation of an accretion disk around the neutron star. Between June 10 and 12, a few days to two weeks before the radio disappearance of the pulsar, the 3–79 keV X-ray spectrum was well fit by a simple power law with a photon index of $\Gamma = 1.17^{+0.08}_{-0.07}$ (at 90% confidence) with a 3–79 keV luminosity of $7.4 \pm 0.4 \times 10^{32}$ erg s^{-1}. Significant orbital modulation was observed with a modulation fraction of 36% ± 10%. During the October 19–21 observation, the spectrum is described by a softer power law ($\Gamma = 1.66^{+0.06}_{-0.05}$) with an average luminosity of $5.8 \pm 0.2 \times 10^{33}$ erg s^{-1} and a peak luminosity of $\approx 1.2 \times 10^{34}$ erg s^{-1} observed during a flare. No significant orbital modulation was detected. The spectral observations are consistent with previous and current multiwavelength observations and show the hard X-ray power law extending to 79 keV without a spectral break. Sharp-edged, flat-bottomed dips are observed with widths between 30 and 1000 s and ingress and egress timescales of 30–60 s. No change in hardness ratio was observed during the dips. Consecutive dip separations are log-normal in distribution with a typical separation of approximately 400 s. These dips are distinct from dipping activity observed in LMXBs. We compare and contrast these dips to observations of dips and state changes in the similar transition systems PSR J1824−2452I and XSS J1227.0−4859 and discuss possible interpretations based on the transitions in the inner disk.

Key words: pulsars: general – pulsars: individual (PSR J1023+0038) – stars: neutron – X-rays: stars

Online-only material: color figures

1. INTRODUCTION

Millisecond pulsars (MSPs; Backer et al. 1982) are neutron stars with surface magnetic fields $B_{\rm surf} \sim 10^8$–10^9 G and rotation periods $P_{\rm rot} \lesssim 30$ ms that show radio, X-ray, and/or γ-ray pulsations. The theory of recycled pulsars (Radhakrishnan & Srinivasan 1982; Alpar et al. 1982; Bhattacharya & van den Heuvel 1991) suggests that during a low-mass X-ray binary (LMXB) phase, angular momentum is transferred to the pulsar through disk accretion from a binary companion. The consequent addition of angular momentum spins up the pulsar to high angular velocities. Further evolution disrupts the accretion and, as the ionized plasma in the pulsar magnetosphere diminishes, the pulsar may be observed as a radio MSP. In a few systems, the pulsar wind can ablate matter from its companion to form black widow (Fruchter et al. 1990) or redback (see Roberts 2011) systems, sometimes leaving a planetary-mass object (Bailes et al. 2011).

While the pulsar spin-up theory is well supported by the presence of binary companions around most MSPs and the discovery of accretion-induced millisecond X-ray pulsations in LMXBs (Wijnands & van der Klis 1998; see Patruno & Watts 2012 for a review) there is little understanding as to how and when the accretion stops and whether the transition from LMXB to a nonaccreting MSP is swift and irreversible or whether the system flip-flops between the two states before settling into a nonaccreting state (Tauris 2012). Recent observations of two remarkable LMXB–MSP transition systems, PSR J1023+0038 (Archibald et al. 2009) and PSR J1824−2452I (Papitto et al. 2013), were the first evidence of multiple state changes during the transformation.

The source FIRST J102347.6+003841 (later renamed PSR J1023+0038) was initially classified as a magnetic cataclysmic variable by Bond et al. (2002). Thorstensen & Armstrong (2005) suggested that the system was an LMXB before the confirming discovery of a 1.7 ms radio pulsar (Archibald et al. 2009, 2010). The pulsar is in a 4.75 hr orbit with a G-type $\sim 0.2\,M_\odot$ companion. Double-peaked H and He lines in archival Sloan Digital Sky Survey (SDSS) spectra revealed

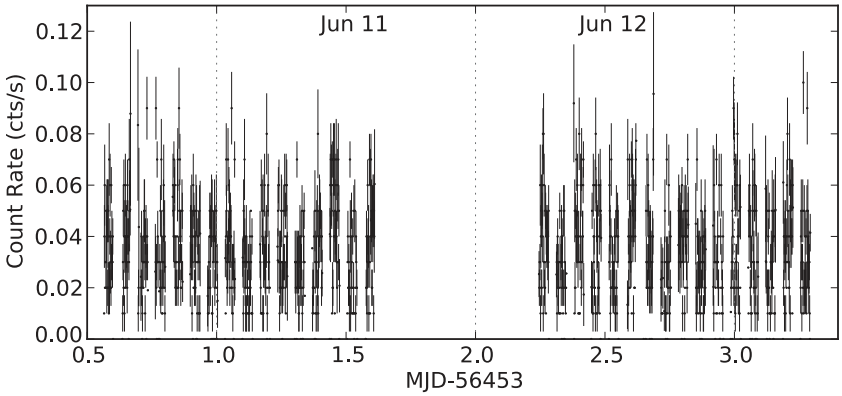

Figure 1. 100 s binned *NuSTAR* light curve of the June observations of PSR J1023+0038 in the 3–79 keV energy range. No flaring activity is observed within this observation window. The periodic gaps in the data are caused by Earth occultation of *NuSTAR*'s line of sight to PSR J1023+0038 through the spacecraft orbit. The dotted vertical black lines separate days of the observation.

that the pulsar had an accretion disk during 2000–2001, but later spectra showed no evidence for accretion (Wang et al. 2009). This conclusion was supported by further optical and X-ray observations (Archibald et al. 2010; Bogdanov et al. 2011). Very Long Baseline Interferometry (VLBI) observations (Deller et al. 2012) of the pulsar allowed the measurement of its parallax distance (1368^{+42}_{-39} pc) and proper motion (17.98 ± 0.05 mas yr^{-1}, 130 ± 4 km s^{-1}). Long-term radio observations and γ-ray measurements have allowed the detailed understanding of the inclination, orientation, and evolution of the system's orbit; the size and temperature of the companion star and estimates for the masses of both of the components (Archibald et al. 2013).

The pulsar has been monitored regularly and detected in the radio bands until recently, indicating the absence of accretion. In observations after 2013 June 15 the radio pulsations had decreased in flux to undetectable levels, accompanied by a 20-fold increase in soft X-ray flux and a five-fold increase in the γ-ray flux (see Stappers et al. 2013; Kong 2013; Stappers et al. 2014; Patruno et al. 2014).

In this paper, we describe *NuSTAR* (Harrison et al. 2013) observations of PSR J1023+0038, the first hard X-ray (3–79 keV) observations of this source. These observations were obtained during its quiescent state in 2013 June, a few days before the pulsar's radio disappearance and later during the accretion phase in 2013 October. This paper is organized as follows. Section 2 describes the details of the observations and X-ray data analysis. In Section 3, we describe the results of the spectroscopic fitting and timing analysis. The astrophysical implications of these results are discussed in Section 4.

2. OBSERVATION AND ANALYSIS

PSR J1023+0038 was first observed by *NuSTAR*[15] between 2013 June 10 and 12 during a prescheduled ≈95 ks observation simultaneous with a ≈4 ks observation with the *Swift* X-ray Telescope (XRT; Burrows et al. 2005). The disappearance of PSR J1023+0038 in radio monitoring was constrained to have occurred between 2013 June 15 and 30 (see Stappers et al. 2014), but the source could not immediately be reobserved by *NuSTAR* due to a solar angle constraint until mid-October. Based on the radio disappearance, a second 100 ks *NuSTAR* observation was scheduled simultaneous with a 10 ks *Swift* observation (described in Patruno et al. 2014) from 2013 October 19 to 21. The details of the observations are summarized in Table 1.

Table 1
Observations of PSR J1023+0038

Obs ID	Start (UT)	End (UT)	Exp (ks)	Rate counts s^{-1}
	NuSTAR			
30001027002	Jun 10 13:15	Jun 10 21:15	13	0.014
30001027003	Jun 10 21:15	Jun 11 14:50	34	0.011
30001027005	Jun 12 05:35	Jun 13 07:30	48	0.012
30001027006	Oct 19 08:00	Oct 21 17:45	100	0.4
	Swift XRT (pphoton counting mode)			
00080035001	Jun 10 14:03	Jun 10 16:11	2.0	0.008
00080035002	Jun 12 22:03	Jun 13 00:00	1.9	0.011
00080035003	Oct 18 05:08	Oct 19 08:38	10	0.23

The preliminary processing and filtering of the *NuSTAR* event data was performed with the standard *NuSTAR* pipeline version 1.2.0 and *HEASOFT* version 6.14. The source was clearly detected at each epoch. We used the `barycorr` tool to correct the photon arrival times for the orbital motion of the satellite and the Earth. The source events were extracted within a 20 pixel (49″, compared to a half-power diameter of 58″) radius around the centroid, and suitable background regions were used. Spectra were extracted using the `nuproducts` script. Using `grppha`, all photons below channel 35 (3 keV) and above channel 1935 (79 keV) were flagged as bad, and all good photons were binned in energy to achieve a minimum of 30 photons per bin.

Similarly, the *Swift* XRT data were processed with the standard `xrtpipeline`, and the photon arrival times were corrected using `barycorr`. The `xrtproducts` script was used to extract spectra and light curves within a radius of 25 pixels (59″). Photons in channels 0–29 (energy <0.3 keV) were ignored, and all channels between 0.3 and 10 keV were binned to ensure a minimum of 30 photons per bin.

3. RESULTS

3.1. June Observations

The *NuSTAR* observation of PSR J1023+0038 in 2013 June detected the source with an average count rate of

[15] *NuSTAR* is a 3–79 keV focusing hard X-ray mission. It consists of two identical coaligned Wolter-I telescopes with CdZnTe detectors at the focal planes. The telescopes provide a point-spread function with a full width at half maximum of 18″and a half-power diameter of 58″over a field of view of 12′×12′. The energy resolution varies from 0.4 keV at 6 keV to 0.9 keV at 60 keV. The data from the two telescopes' focal plane modules are labeled FPMA and FPMB.

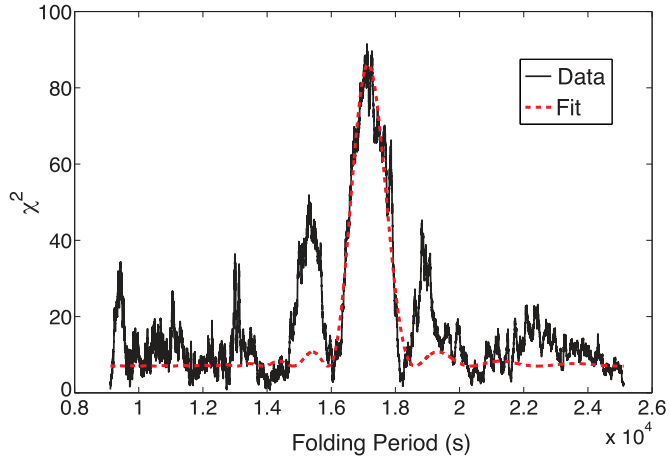

Figure 2. χ^2 test and epoch folding in searching for the binary-system orbital period with *NuSTAR* June data in the 3–79 keV energy range. The solid black line is the χ^2 of the folded observation data with respect to a null hypothesis as a function of folding period (i.e., test orbital period), and the red dashed line is the best fit of the data with the χ^2 variation expected from a sinusoidal waveform (Leahy 1987). The χ^2 distribution has 7 dof.

(A color version of this figure is available in the online journal.)

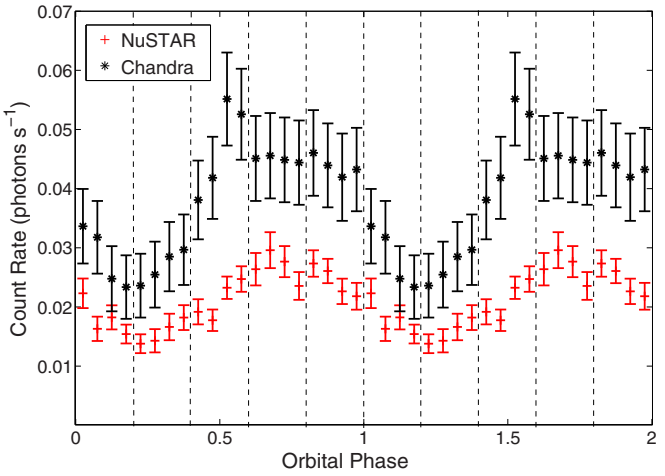

Figure 3. Orbital modulation from PSR J1023+0038 in the 3–79 keV energy range in the 2013 June observation (red "+"). The corresponding 0.3–8 keV *Chandra* orbital modulation (black "*"; Bogdanov et al. 2011) is overlaid. The `barycorr` corrected photons from FPMA and FPMB were folded with the best-fit period 17147.78 s. The orbital modulation is plotted for two orbits for clarity.

(A color version of this figure is available in the online journal.)

0.012 counts s^{-1} combined in FPMA and FPMB. No significant flaring or dipping activity was observed (Figure 1).

3.1.1. Timing Analysis

We searched for orbital modulation by folding the `barycorr`-corrected photons into eight orbital phase bins with various trial orbital periods around the nominal period of 17,100 s (4.75 hr). A range of orbital periods between 9000 s and 25,000 s (2.5–7 hr) were used with a step size of 1 s. We used the epoch-folding statistical method (Leahy 1987) to fit the χ^2 of the folded June observation data with respect to a null hypothesis. We detected the orbital modulation at a significance of $\approx 21\sigma$. After fitting (Figure 2), the best-fit orbital period is 17148 $\pm$ 83 s. This is consistent with the 17115.52524(3) s orbital period measured from long-term radio monitoring (Archibald et al. 2013). Varying the number of orbital phase bins and step sizes for orbital periods led to the same result.

We folded the photons recorded in both the FPMA and FPMB detectors with the best-fit period to create an orbital modulation profile (Figure 3). The modulation fraction, defined as $(F_{\rm max} - F_{\rm min})/(F_{\rm max} + F_{\rm min})$, where $F_{\rm max}$ and $F_{\rm min}$ are the maximum and minimum photon fluxes, respectively, is 36% $\pm$ 10%. The fractional rms modulation, defined as $\sqrt{\langle F^2\rangle - \langle F\rangle^2}/\langle F\rangle$, where the average is taken over all orbital phase bins, is 22%. Compared with the amplitude of 0.0317 $\pm$ 0.0095 counts s^{-1} for the lower energy range observed by *Chandra* in 0.3–8 keV (Bogdanov et al. 2011), the amplitude with *NuSTAR* observation, which is 0.0158 $\pm$ 0.0034 counts s^{-1} in 3–79 keV, is smaller.

We searched for pulsations at the spin period of the pulsar in the *NuSTAR* data in several different ways. First, we note that *NuSTAR*'s onboard clock, which is corrected at every ground pass, has exhibited residual timing jumps of 1–2 ms at unpredictable times on timescales of days to months (K. Madsen et al., in preparation); this makes a pulsation search at the 1.7 ms period of PSR J1023+0038 problematic. Nevertheless, recognizing that there could, in principle, be some spans in which the clock is sufficiently stable to detect bright pulsations and that a short-term pulsation search may be more likely to succeed than a long-term search, we proceeded to search as described below.

In all cases, we used the `PREPFOLD` facility within the `PRESTO` suite of pulsar search software to fold the data set into 20 phase bins using spin and orbital parameters nominally determined from radio timing 2013 pre-June (see Archibald et al. 2013). Each search described below was done for three energy ranges: 3–79 keV, 3–10 keV, and 10–79 keV, and the June and October data were analyzed separately.

First, we folded each of the June and October data sets at the nominal ephemeris. In addition, to maintain full sensitivity given the known orbital period variations (see Archibald et al. 2013), we searched in $T0$ (the epoch of periastron) space by varying it ± 10 s around its nominal value in steps of 0.2 s, folding at each trial value. The largest $T0$ error in this grid, 0.1 s, corresponds to a 1.5% error in rotational phase for our searches and is well below the uncertainties due to observed systematic timing variations.

We also searched for a pulse in smaller time spans: we broke the June and October data into sequences of duration equal to the orbital period of the binary. Each sequence was further divided into six equal parts. We individually folded and searched each of these parts for pulsations. Also, parts at the same orbital phase were combined in each of the June and October data sets separately, and the combinations were searched. We repeated the same searches using 12 equal orbital phase sections. In total, we searched more than ten thousand parameter combinations, using reduced χ^2 statistics. Accounting for the number of trials, we found no significant pulsations.

3.1.2. Spectral Analysis

The *Swift* XRT and *NuSTAR* spectra of PSR J1023+0038 were fitted with an absorbed power-law model (`const*tbabs*powerlaw` in `XSPEC`; Figure 4). The source was barely detected in the *Swift* XRT observations `00080035001` and `00080035002` in June with 0.3–10 keV count rates of $\lesssim 10^{-2}$ counts s^{-1}. We added the two exposures to improve the signal-to-noise ratio. These observations were only used to constrain the estimate of the column density $N_{\rm H}$ during the June observation because *NuSTAR* data alone are not very sensitive to relatively low column densities. We constrained $N_{\rm H} < 2.8 \times 10^{21}$ cm^{-2}

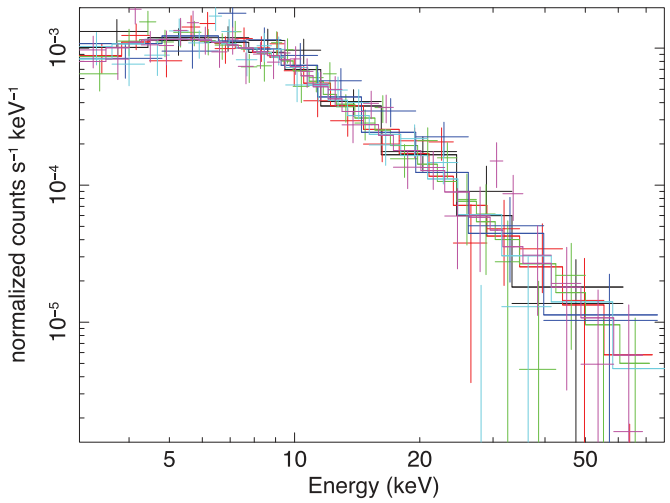

Figure 4. Power-law fit to June *NuSTAR* observations. The data sets 30001027002, 30001027003, and 30001027005 were fit simultaneously with the same model to improve signal-to-noise ratio. Column density was undetectable and hence set to zero. The data from the two *NuSTAR* detectors FPMA and FPMB were linked by a floating cross-normalization constant. The fit achieved χ^2/dof = 113.4/117. The correspondence between colors (in the electronic version of the manuscript) and spectra are as follows: black:30001027002 FPMA, red:30001027003 FPMA, green:30001027005 FPMA, blue:30001027002 FPMB, cyan:30001027003 FPMB, and magenta:30001027005 FPMB.

(A color version of this figure is available in the online journal.)

Table 2
NuSTAR Spectra During 2013 June

Parameter	Observation (30001027xxx)			
	002	003	005	Average
C_{FPMB}[a]	$1.10^{+0.23}_{-0.20}$	$1.08^{+0.16}_{-0.14}$	$1.10^{+0.13}_{-0.12}$	$1.087^{+0.092}_{-0.085}$
Γ ($N_H = 0$)	$1.00^{+0.18}_{-0.17}$	$1.26^{+0.13}_{-0.12}$	$1.15^{+0.10}_{-0.10}$	$1.17^{+0.08}_{-0.07}$
$\log_{10}(F_X)$[b]	$-11.34^{+0.10}_{-0.10}$	$-11.55^{+0.07}_{-0.08}$	$-11.47^{+0.06}_{-0.07}$	$-11.48^{+0.05}_{-0.05}$
χ^2/dof	10.9/16	46.57/41	48.14/57	113.4/117

Notes.
[a] Scaling constant for FPMB data as compared to FPMA data.
[b] 3–79 keV flux in units of erg cm^{-2} s^{-1}.

(3σ), which is consistent with measurements by Bogdanov et al. (2011) and Archibald et al. (2010). Setting $N_H = 0$ did not change the best-fit values of power-law index Γ and the integrated flux; hence, N_H was frozen to zero for all future fits of the June data. No significant emission or absorption features are observed in the spectra. The thermal emission contribution observed by Bogdanov et al. (2011) with $kT \approx 0.55$–0.75 keV is too faint in the 3–79 keV band to be observed by *NuSTAR*.

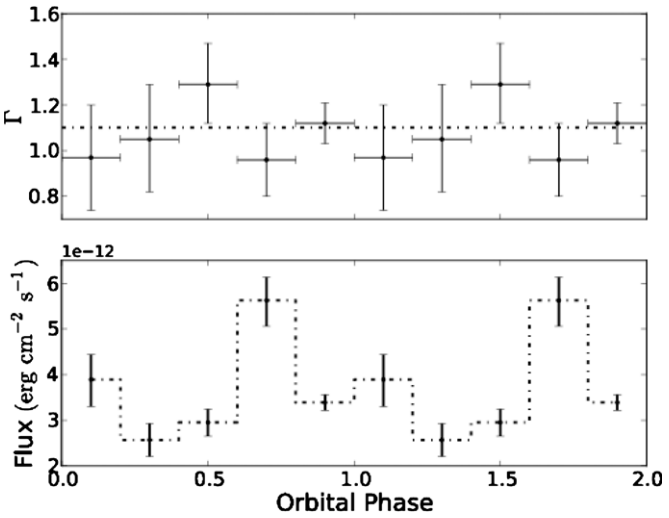

Figure 5. Top panel: variation of power-law index (Γ) as a function of orbital phase for the combined June spectrum. Two orbits are shown for clarity. Black dots indicate best-fit values. All error bars are 90% confidence. The dash-dotted lines indicate the error-weighted average of $\Gamma = 1.10$. The integrated 3–79 keV flux from June (bottom panel) is depicted by black dots.

Table 2 shows the measured values of Γ and 3–79 keV flux from the three June observations. The error bars are quoted at 90% confidence. In subsequent analyses, the observations were simultaneously fit with a single model to improve the signal-to-noise ratio. The combined fit values are $\Gamma = 1.17^{+0.08}_{-0.07}$ and $F_X = 3.3 \pm 0.16 \times 10^{-12}$ erg cm^{-2} s^{-1}, corresponding to a 3–79 keV luminosity of $7.4 \pm 0.4 \times 10^{32}$ erg s^{-1} at PSR J1023+0038's measured distance. The fit achieved a χ^2 of 113.4 with 117 degrees of freedom (dof).

3.1.3. Orbital Modulation of Spectra

To analyze the spectral variations during the orbit, we set *good-time-interval* (GTI) windows for orbital phases: 0.0–0.2, 0.2–0.4, 0.4–0.6, 0.6–0.8, and 0.8–1.0. To improve the signal of the phase-resolved spectra from the June observation, we summed up the events from *NuSTAR* observations 30001027002, 30001027003, and 30001027005. The five phase-resolved spectra extracted were fitted with an absorbed power-law model. From the previous discussion, the absorption column value was frozen to $N_H = 0$. The power-law index Γ and normalization were allowed to vary for each phase. Table 3 and Figure 5 list and plot the best-fit values for Γ and the integrated X-ray fluxes measured for the five orbital phases. The errors are quoted at 90% confidence. The measurements are consistent with a constant Γ value over the orbital phase with an error-weighted average of 1.10 ± 0.12.

Table 3
Orbital Variation of Spectral Fits in June[a]

Parameter	Orbital Phase				
	0.0–0.2	0.2–0.4	0.4–0.6	0.6–0.8	0.8–1.0
PL index ($N_H = 0$)	$0.97^{+0.23}_{-0.23}$	$1.05^{+0.24}_{-0.23}$	$1.29^{+0.18}_{-0.17}$	$0.96^{+0.16}_{-0.16}$	$1.12^{+0.09}_{-0.09}$
$\log_{10}$(flux)[b]	$-11.41^{+0.14}_{-0.15}$	$-11.59^{+0.14}_{-0.14}$	$-11.53^{+0.10}_{-0.10}$	$-11.25^{+0.09}_{-0.10}$	$-11.47^{+0.05}_{-0.05}$

Notes.
[a] Spectra from observations 2, 3, and 5 were combined. Column density was undetectable and hence set to zero. The fit achieved χ^2/dof = 127.99/150.
[b] 3–79 keV flux in units of erg cm^{-2} s^{-1}.

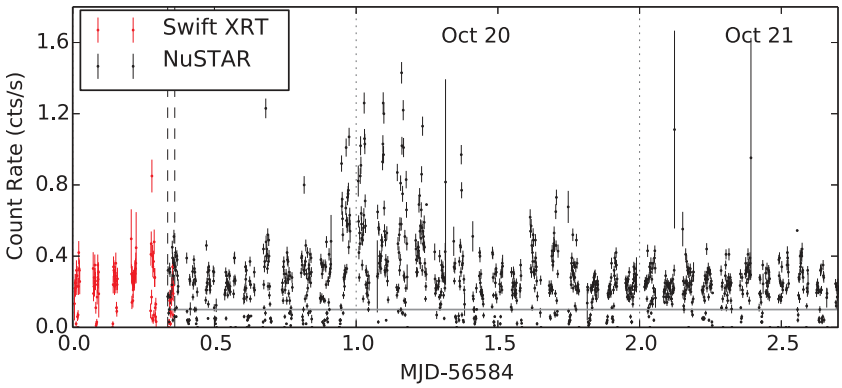

Figure 6. 100 s binned light curve from 0.3–10 keV from *Swift* (red points) and 3–79 keV from *NuSTAR* (black points) observations. For clarity, *NuSTAR* FPMA and FPMB observations are averaged. The average count rate during the ≈10 hr long flare is factor of five higher than the out-of-flare count rate. The gray horizontal line at 0.1 counts s^{-1} denotes low flux levels seen in the *NuSTAR* observations discussed in detail in Section 3.2.4. Two vertical dashed black lines denote the ≈30 minute overlap in the *Swift* and *NuSTAR* observations. Dotted black vertical lines divide the UTC dates of the observations, as noted at the top of the plot. The gaps in observations are due to Earth occultations.

(A color version of this figure is available in the online journal.)

Table 4
2013 June Spectra Compared to Archival Measurements

Reference	Inst./Band (keV)	Γ	Flux (10^{-13} erg cm^{-2} s^{-1})	
			Meas.[a]	Extrap.[b]
Homer et al. (2006)	*XMM-Newton*/(0.01–10)	1.27 ± 0.03	5.3 ± 0.6	6.3 ± 0.5
Archibald et al. (2010)	*XMM-Newton*/(0.5–10)	0.99 ± 0.11	4.9 ± 0.3	5.8 ± 0.4
Bogdanov et al. (2011)	*Chandra*/(0.3–8)	1.00 ± 0.08	4.0 ± 0.14	4.9 ± 0.4

Notes. The flux errors do not include the systematic cross-normalization error.
[a] Measured flux from only the nonthermal emission after separating the thermal soft-X-ray component, if any.
[b] Extrapolated into the instrument's band from measured *NuSTAR* power law.

3.1.4. Comparison with Archival Data

We compare the flux measured in June to archival measurements by Homer et al. (2006), Archibald et al. (2010) and Bogdanov et al. (2011; Table 4) by extrapolating the *NuSTAR* power law to lower energies. From the archival spectral fits, we extract the flux expected from the nonthermal power law because the soft thermal component is negligible in the *NuSTAR* energy band. We find that the fluxes are consistent within the expected cross-normalization errors (Madsen et al., in preparation). Along with the detection of the radio MSP, this strongly suggests that on 2013 June 10 and 12 PSR J1023+0038 was in the same state with no accretion disk observed since 2004.

3.2. October Observations

Figure 6 shows the *Swift* XRT and *NuSTAR* light curves during the October observations averaged over 100 s bins. The two vertical dashed lines denote the ≈30 min overlap in the *Swift* and *NuSTAR* observations. During the *NuSTAR* observations, we observed a flare for a period of ≈10 hr with a factor of five increase in X-ray flux. Binning the same light curve in 1200 s bins, we observed a factor of 25 variations in the count rate within 1 hr (three bin points). In the analysis that follows, we analyze the data with and without excision of the flare data.

3.2.1. Timing Analysis

We searched for the orbital modulation of X-rays from PSR J1023+0038 using the same methodology as for the June data (Figures 2 and 3). We folded the entire data set, as well as a subset for which flares and dips were excised, at a range of orbital periods centered around the value measured in June; however, as shown in Figure 7, practically all trial periods yielded a value of χ^2 inconsistent with the null hypothesis. This is in strong contrast to what we observed in June (Figures 2

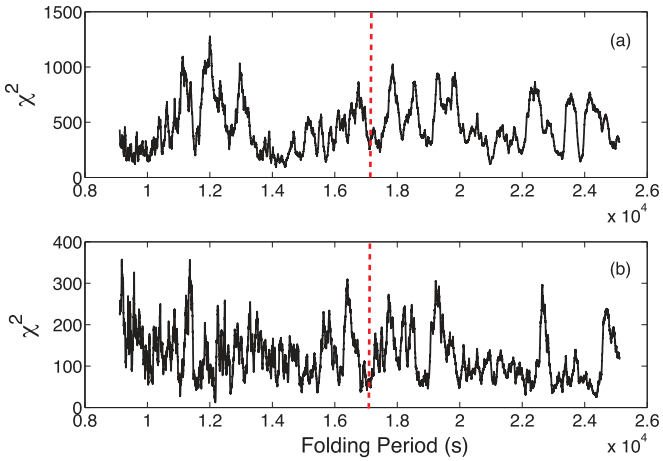

Figure 7. Top panel: χ^2 test and epoch folding in searching for the binary-system orbital period with *NuSTAR* October data in the 3–79 keV energy range. The analysis is the same as done for the June data in Figure 2. The solid black line is the χ^2 of the folded observation data with respect to a null hypothesis as a function of trial orbital periods, and the red dashed line is the location of the peak measured in the June data. The χ^2 distribution has 7 dof. Bottom panel: same plot as above after excising the time periods with flares and dips. Although significant variation exists, mostly due to the flaring activity and variability, no clear signal of orbital period is observed.

(A color version of this figure is available in the online journal.)

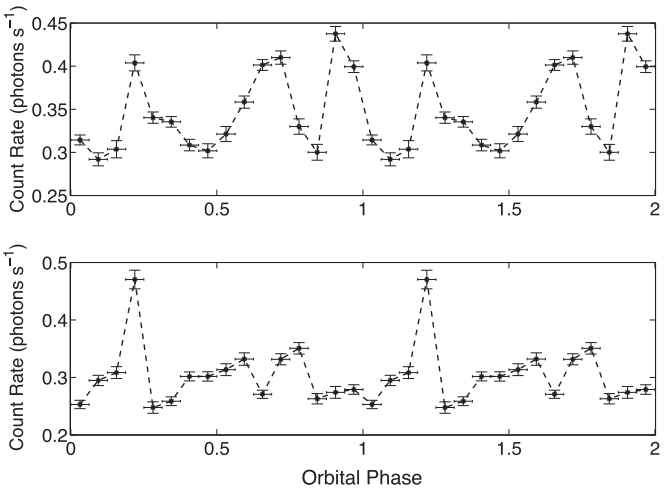

Figure 8. Top panel: light curve of October data in the 3–79 keV energy range as a function of orbital phase, folded with the best-fit period of 17147.78 s from 2013 June. Bottom panel: same plot after excising the time periods with flares and dips. No significant coherent sinusoidal modulation is observed. Although significant variability is observed, it is not related to the orbit because such variability is observed regardless of folding period, as is clear from the lack of a clear maxima in Figure 7.

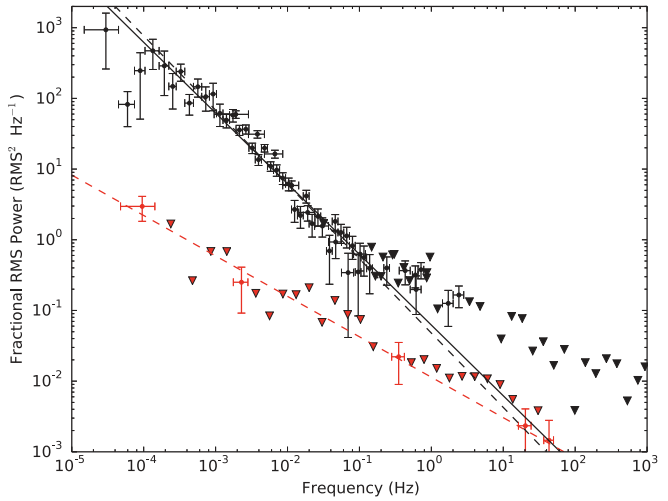

Figure 9. Power spectral distribution (PSD) of PSR J1023+0038 in October (black dots) normalized with the prescription of Miyamoto et al. (1991). The inverted black triangles indicate 3σ upper limits on the power spectrum. The PSD is well fit by a red noise (flicker) power law, $P(f) \propto f^{-1}$ (solid black line). If the power-law index is allowed to vary, the fit ($P(f) \propto f^{-1.05\pm0.05}$, dashed black line) is consistent with the flicker noise. Similarly, red dots and red inverted triangles denote the PSD during the June observations. The best-fit power law is $P(f) \propto f^{-0.57\pm0.03}$ (red dashed line).

(A color version of this figure is available in the online journal.)

and 3); in October, by contrast, we detect no evidence for orbital modulation. We folded the photons detected in both the FPMA and FPMB detectors with the best-fit period of 17,148 s measured in 2013 June to create an orbital modulation profile (Figure 8), which also does not reveal coherent modulations, with or without the flare and dip data. We used a histogram of the measured χ^2 values for the range searched and found the value of χ^2 higher than 99% of all other values. We then use the analytical formulae relating the amplitude and χ^2 (Leahy et al. 1983) to derive an upper limit for the pulsed amplitude of $\approx$0.6 counts s^{-1} in the 3–79 keV band. However, we note that this estimate is only approximate because the Leahy et al. (1983) formulae assume that no significant power is present in

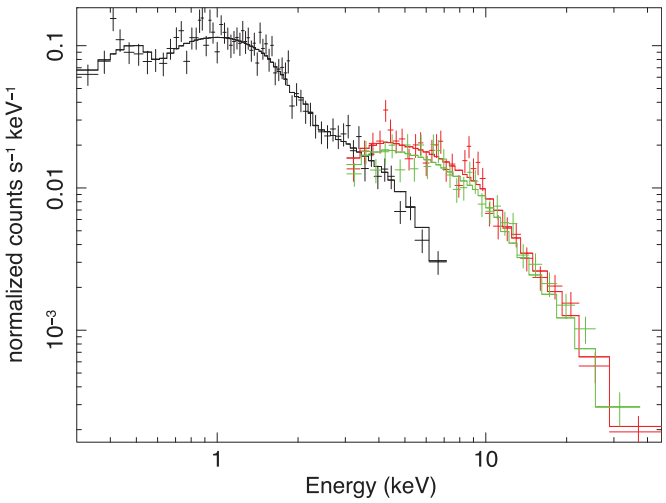

Figure 10. Combined absorbed power-law fit to October observations with *Swift* XRT spectrum 00080035003 (black) and *NuSTAR* spectrum 30001027006 (FPMA in red and FPMB in green). $N_{\rm H}$ was allowed to vary and achieved a best-fit value of $2.9^{+1.5}_{-1.3} \times 10^{20}$ cm^{-2} with $\Gamma = 1.66^{+0.06}_{-0.05}$, consistent with Patruno et al. (2014). The fit achieved χ^2/dof = 120.55/124.

(A color version of this figure is available in the online journal.)

the data, apart from the signal of interest, which is obviously not true in this case. A true upper limit is difficult to determine without more prior knowledge regarding the statistical nature of the strong variability observed.

In order to look for other periodicities or quasi-periodic oscillations sometimes observed in other LMXBs, we binned the photon event time series from the source and the background regions in 500 μs time bins and performed a Fourier transform to obtain the power spectrum of PSR J1023+0038. We used the fractional rms normalization prescribed by Miyamoto et al. (1991) such that the power spectrum is expressed in units of (rms mean^{-1})^2 Hz^{-1}. The expected Poisson rate was subtracted. We verified that the dead-time corrected light curves showed the expected Poisson variations at high frequencies in the background and source power spectra. Figure 9 shows the power spectrum of PSR J1023+0038 in October (black dots) and upper limits (black inverted triangles) compared to that in June (red dots and inverted triangles). We fit a red flicker noise power-law spectrum ($P(f) \propto f^{-1}$, black line) between $f = 3 \times 10^{-4}$–5×10^{-1} Hz. While the standard χ^2 value is 51 in 30 dof, using the Whittle statistic as discussed by Barret & Vaughan (2012) gives a value of 190 for 30 dof. However, it is to be noted that the interpretation of these fits is not definitive for small number of degrees of freedom. The integrated fractional rms variation in the abovementioned frequency band is 65%, and the residual fractional rms variation after subtracting the flicker noise component is 18%. If the red-noise power-law index is allowed to vary, the best-fit power law is $P(f) \propto f^{-1.05\pm0.05}$ (black dashed line), consistent with the flicker noise; however, the best-fit power law to the June power spectrum is $P(f) \propto f^{-0.57\pm0.03}$ (red dashed line). We do not see any significant features in the power spectrum.

Using the same procedures described in Section 3.1.1, no X-ray pulsations at the pulsar spin period were detected in the October data.

3.2.2. Spectral Analysis

The *Swift* XRT data and the first $\approx$ four hr of *NuSTAR* data were jointly fit (Figure 10) with an absorbed power-law model.

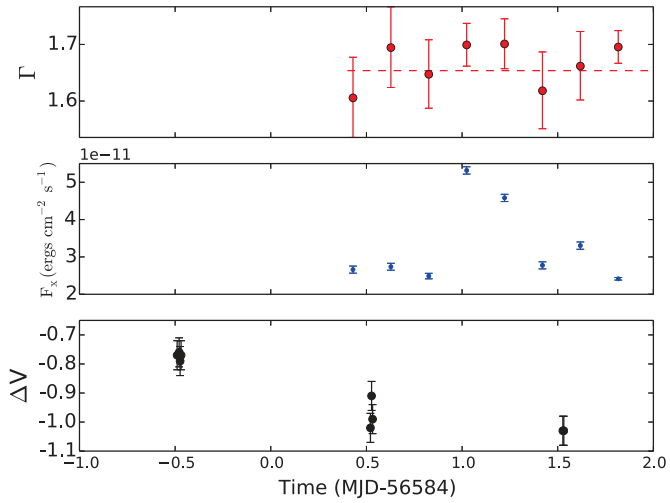

Figure 11. Top panel: variation of power-law index Γ as a function of time during the *NuSTAR* October observation. Each data point is averaged over one orbital period to eliminate the effect of orbital modulation. The dashed line is the weighted average value of Γ = 1.654. There is no statistically significant change in Γ before, during, or after the flare. Middle panel: variation of 3–79 keV X-ray flux measured by *NuSTAR* as a function of time. The flare is seen as a factor of two increase in flux at MJD = 56585. Bottom panel: corresponding variation in optical magnitude at the same orbital phase as a function of time. The data are from Halpern et al. (2013). Due to the sparse monitoring, we do not have observations during the flare. However, the pre- and postflare optical observations are consistent within the error bars.

(A color version of this figure is available in the online journal.)

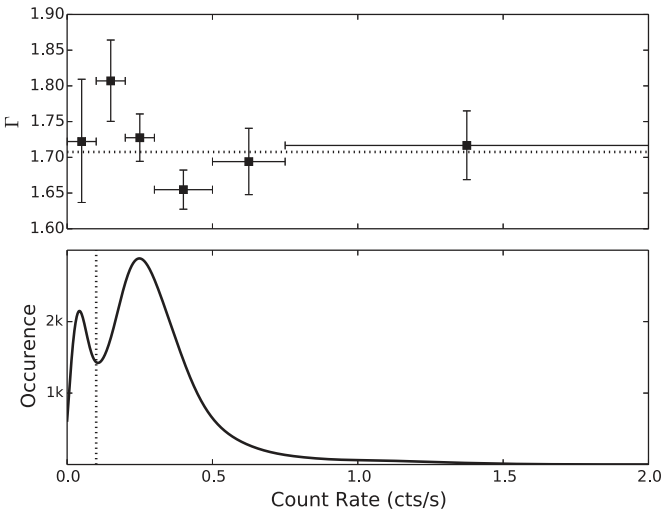

Figure 12. Top panel: variation of photon PL index Γ as a function of photon count rate. The photon count rates are binned between 0–0.1, 0.1–0.2, 0.2–0.3, 0.3–0.5, 0.5–0.7, and 0.7–2.0 counts s^{-1}. Γ varies only by 0.15 over a factor of seven change in count rate. We detect a minor variation in the 0.1–0.2 counts s^{-1} bin (transition between the two states) above a constant value (dotted line). Bottom panel: the distribution of count rates in the 100 s binned *NuSTAR* light curve (FPMA + FPMB) smoothed and weighted by the measurement errors. The dotted vertical line shows the demarcation between the two distinct flux states that are seen.

The cross-normalization constants between *Swift* XRT and *NuSTAR* FPMA and FPMB modules were allowed to vary. The best-fitting parameter values were $N_{\rm H} = 2.9^{+1.5}_{-1.3} \times 10^{20}$ cm^{-2}, which is nominally consistent with the June spectra, $\Gamma = 1.66^{+0.06}_{-0.05}$, with 3–79 keV $F_X = 2.61 \pm 0.06 \times 10^{-11}$ erg cm^{-2} s^{-1}, and achieved a χ^2/dof = 120.55/124. The corresponding luminosity is $5.8 \pm 0.2 \times 10^{33}$ erg s^{-1}.

In order to analyze the count-rate variation during the flare, we divided the *NuSTAR* October observation into eight segments, each covering one orbital period of the system, to eliminate any variation due to orbital modulation. We extracted spectra and fit an absorbed power law to the measurements. We froze the value of the column density $N_{\rm H} = 3.8 \times 10^{20}$ cm^{-2} from the corresponding *Swift* observations (Patruno et al. 2014). Figure 11 shows the variation of the power-law index Γ and X-ray flux as a function of time. The corresponding variation in optical magnitude (Halpern et al. 2013) is also plotted. Due to the sparse monitoring, there are no optical observations during the flare. However, the preflare and postflare optical brightness of the system is constrained to be almost equal.

3.2.3. Spectral Variations with Count Rate

In order to analyze the variation in brightness, we created `GTI` windows by filtering the 100 s light curve data points into six count-rate ranges: 0–0.1 counts s^{-1}, 0.1–0.2 counts s^{-1}, 0.2–0.3 counts s^{-1}, 0.3–0.5 counts s^{-1}, 0.5–0.7 counts s^{-1}, and 0.7–2 counts s^{-1}. We then re-extracted the spectra within the `GTIs` using the *NuSTAR* pipeline. The spectra are well fit by a PL model similar to the averaged spectra. The value of $N_{\rm H}$ was frozen to 3.8×10^{20} cm^{-2}.

Figure 12 shows the variation of the 3–79 keV flux and photon power-law (PL) index Γ as a function of count rate. There is weak evidence that the spectrum is harder at higher count rates, but the measurements of Γ are consistent with a constant value over the four count-rate ranges. The bottom panel of Figure 12 shows a distribution of the count rates (weighted and smoothed by the measurement errors) from the 100 s binned light curve. There is clear evidence for two distinct states. The vertical dotted line shows the approximate count rate (0.1 counts s^{-1}) that demarcates the two states. These two states occur due to sharp dips in the light curve, as described below.

3.2.4. Short Timescale Dips in the Light Curve

Apart from the 10 hr flare, significant short timescale variations are observed during the October *NuSTAR* and *Swift* observations (see Patruno et al. 2014, for *Swift* XRT flickering). In this section, we present a detailed phenomenological description of the variations. Figure 13 shows three examples of dips observed in the count rate binned in 100 s bins. The dips are not periodic or uniform in depth and width. In order to understand the nature of these variations, the photons were divided into low-energy (3–7.5 keV) and high-energy (7.5–79 keV) bands.

In order to quantitatively analyze the occurrence of these dips, we created a normalized light curve by dividing a 30 s binned light curve (of 3–79 keV photons) with a light curve smoothed over a long timescale (600 s). We verified that changing the smoothing timescale between 600 s and 1800 s led to consistent results. The dips were defined as time periods when the normalized count rate was less than 0.5. This threshold was determined by visual inspection of the normalized light curve and is insensitive to small variations (0.45–0.55). The dip periods thus extracted were smoothed with a binary closing function (adapted from image processing; see Gonzalez & Woods 1992; using the `scipy.ndimage` library) to exclude small-amplitude, single-bin spikes in wide (>four bins) dips. The widths and positions of all other dips remain unaffected by this smoothing function.

We observed 224 dips in the entire observing sequence. To calculate the temporal positions of the centers of the dips in the normalized light curve, we converted the normalized light curve

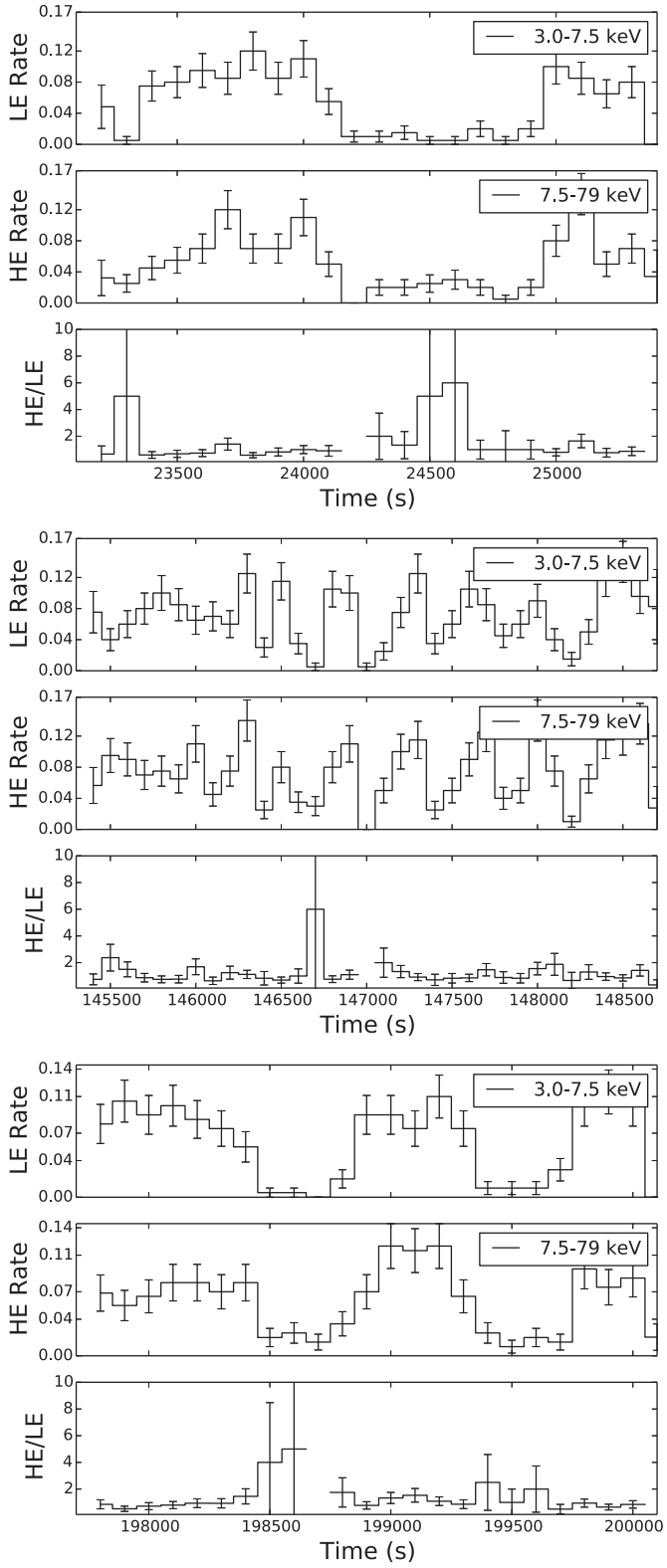

Figure 13. Representative light curves from the October *NuSTAR* observation of PSR J1023+0038. In each figure, the top panel shows the low-energy (3.0–7.5 keV) count rate, the middle panel shows the high-energy (7.5–79 keV) count rate, and the bottom panel shows the hardness ratio between the two energy bands. The hardness ratio is statistically constant unlike in dips observed in similar accreting systems. Each data point is averaged over 100 s time bins. The *x*-axis is time marked in seconds from the beginning of observation, October 19 08:00:04 UTC.

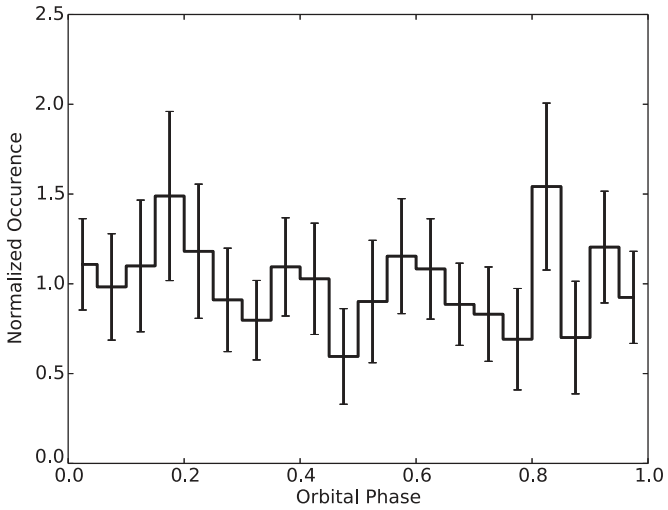

Figure 14. Histogram of orbital phase distribution of dip centers. The distribution is normalized by the orbital phase coverage of the data, which is uneven due to the near 1:3 ratio between the *NuSTAR* orbital period (≈1.5 hr) and the binary orbital period and the Earth occultations that interrupt observations every half revolution. The data are consistent with being uniformly distributed through orbital phases.

into a binary dip–nondip light curve where the dip time points were marked as one and the nondip timepoints were marked as zero. The temporal positions of the dips were calculated by using a segmenting function to identify separate dips and using a center-of-mass function to calculate the central position of each dip segment. We converted the temporal positions into orbital phases using the orbital ephemeris described in the timing analysis.[16] We created a histogram of the observed dip position as a function of binary orbital phase (Figure 14). We divided each phase bin with the orbital coverage in that phase bin, and the overall ratio was normalized to unity. Figure 14 shows no significant preference in dip time for a specific orbital phase bin. The dips are thus uniformly and randomly distributed with orbital phase and do not show any obvious relationship to the system's orbit. Similarly, a search for periodicity in the dip occurrences did not reveal any significant signal.

A histogram of the separations between consecutive dips is shown in Figure 15. The distribution is well fit by a log-normal distribution with a probability distribution function defined as

$$P(x;\, A,\, \mu,\, \sigma)dx = \frac{A}{x\sigma\sqrt{2\pi}} \exp\left(-\frac{(\log x - \mu)^2}{2\sigma^2}\right) dx, \quad (1)$$

where x is the separation of consecutive dips, A is the normalization factor, μ is the location parameter or the mean of $\log x$, and σ is the scale factor of the distribution. We measure $\exp(\mu) = 365 \pm 3$ s and $\sigma = 0.48 \pm 0.04$.

Similarly, a histogram of the dip widths (Figure 16) shows a sharp decline in the distribution as a function of dip width. The dips are well fit by a power law $P(x) \propto x^{-\alpha}$ where x is the width of the dips in seconds. The best-fit value of α was measured to be 1.73 ± 0.07. The corresponding fit is shown as a dashed line in Figure 16. An exponential fit to the distribution leads to a less significant fit (dotted line) with a best-fit timescale of 42 ± 5 s. Due to our smoothing function, we do not consider dips smaller

[16] We used $T0 = 55361.592856125$ MJD and $P_{\rm orb} = 17115.52238$ s. The 10–20 s drifting of the $T0$ described in the timing analysis is too small to affect this analysis.

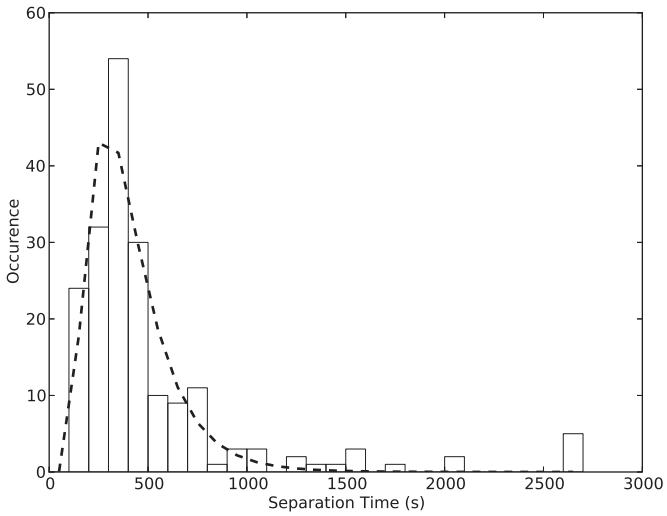

Figure 15. Histogram of separations between the dip centers. The observations are well fit by a log-normal distribution with mean separation of 365 ± 3 s and a scale factor of 0.48 ± 0.04 (see Section 3.2.4 for a description of the parameters).

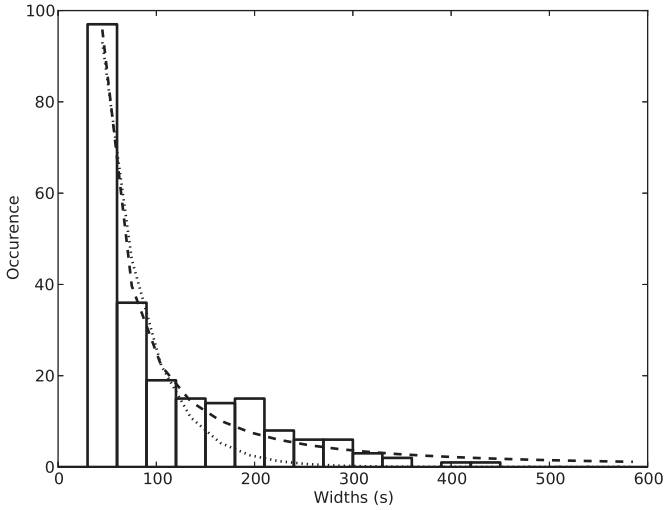

Figure 16. Histogram of widths of the dips. The observations are fit by a power law (dashed line) with an index of 1.73 ± 0.07 with a reduced $\chi^2 = 1.3$ with 17 dof. An exponential law with a timescale of 42 ± 5 s (dotted line) may be fit, but the resulting χ^2 is much worse (reduced $\chi^2 \approx 32$, with 17 dof) because it underestimates the occurrence of dips with widths of 200–300 s. The lowest timescales have been excised from the fit to prevent statistical biasing from the smoothing algorithm described in the text.

than 60 s in the fitting. The widths of the dips are not correlated with the separation to the preceding or successive dip.

We converted the dip locations into timing windows for the `xronos` task `powspec` and extracted the power spectrum during the dip states. We also created a power spectrum for the nondip windows of the light curve. To avoid the variations caused by different Fourier windows, we chose contiguous intervals of 60 s length and averaged the power spectra. Both of the power spectra (Figure 17) were normalized using the normalization prescribed by Leahy et al. (1983). We do not observe any significant difference in the photon rate during the dip state as compared to the nondip state.

4. DISCUSSION

We have presented 3–79 keV observations of the MSP-LMXB transition system PSR J1023+0038 before and

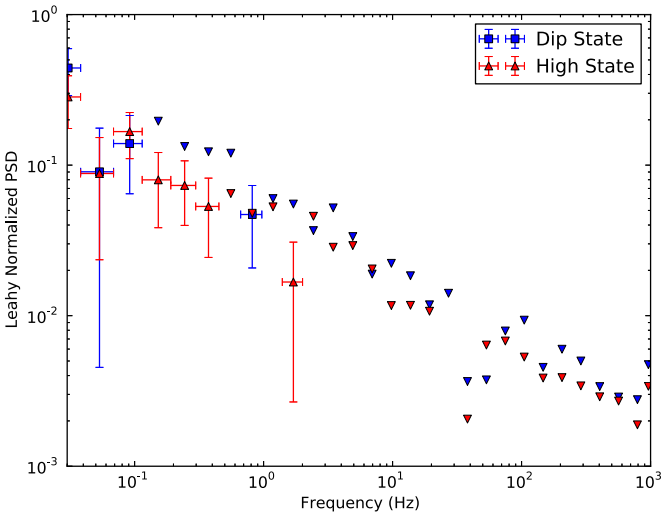

Figure 17. PSD of PSR J1023+0038 during dips (blue squares) and outside of dips (red triangles) normalized with the prescription of Leahy et al. (1983). Inverted blue and red triangles indicate 3σ upper limits for the PSD during dips and outside of the dips, respectively. The two power spectra are statistically the same.

(A color version of this figure is available in the online journal.)

after the 2013 June 15–30 establishment of an accretion disk around the pulsar with phase-resolved spectral and timing analyses. We have observed the 3–79 keV luminosity of the system increase from 7.4×10^{32} erg s^{-1} to 6.0×10^{33} erg s^{-1} between 2013 June 10–12 (a few days to two weeks before the transition) and 2013 October 19–21. These luminosities, being much lower than the 10^{35-37} erg s^{-1} luminosity typical of accreting LMXBs, are consistent with the previously proposed idea that Roche lobe overflow has occurred and an accretion disk has formed, but the in-falling matter has been prevented from accreting onto the pulsar surface and is now surrounding the pulsar (see Stappers et al. 2013, 2014; Kong 2013; Halpern et al. 2013; Patruno et al. 2014).

In order to perform a multiwavelength comparison of the pre- and post-transition behavior, we compiled all published and new data into a spectral energy distribution (SED) from UV to γ-rays (Figure 18), augmenting the SED reported by Takata et al. (2014). The pretransition (June) spectrum from *NuSTAR* and the presence of deep orbital modulations is similar to the X-ray observations from 2004 to 2010 (Homer et al. 2006; Archibald et al. 2010; Tam et al. 2010; Bogdanov et al. 2011) and is consistent with the hard X-rays being emitted by synchrotron emission from the intrabinary shock as suggested by Bogdanov et al. (2011). This similarity along with the sudden change in *Fermi*-LAT γ-ray flux in June (Stappers et al. 2014) argues that the system in June was still in the diskless state achieved after its 2000–2001 accretion episode (Wang et al. 2009). Hence, a gradual transition of the X-ray flux is ruled out, consistent with the radio behavior and γ-ray behavior (Stappers et al. 2014).

From the presence of γ-ray emission and the absence of radio pulsations, Stappers et al. (2014) suggested that the pulsar is enshrouded in gaseous material outside the light-cylinder radius of 81 km, held up by the magnetic pressure. Depending on the location of the barrier, the presence of material would prevent either the detection or generation of radio pulses. In the former case, the γ-rays could be emitted from the shock emission of the pulsar wind interacting with the in-falling matter. In the

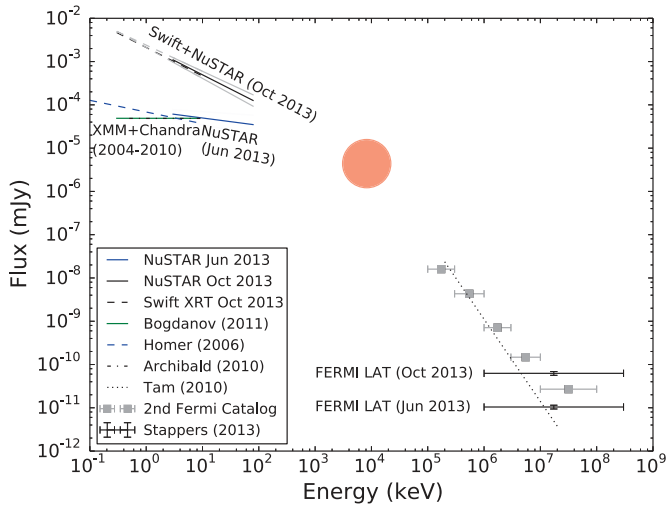

Figure 18. Spectral energy distribution of PSR J1023+0038 from published results and current work. The solid blue lines and the solid black lines in the 3–79 keV band are the power-law fits from the 2013 June and 2013 October *NuSTAR* observations respectively. The light blue and gray solid lines denote the corresponding uncertainties at 90% confidence. Black error bars denote June and October flux estimates from *Fermi*-LAT in the 1–300 GeV band from Stappers et al. (2014), which assumes $\Gamma = 2.5$. The gray squares are photon fluxes from the *Fermi*-LAT second source catalog (Nolan et al. 2012). The red circle is the approximate location of a possible crossover of the hard X-ray and γ-ray power law, at a photon energy of about 1–10 MeV.

(A color version of this figure is available in the online journal.)

latter case, the γ-ray emission may occur, in some models, via shocks in a leptonic jet ejected by the propeller mechanism, as suggested by Papitto et al. (2014b) for the case of the LMXB-like state of XSS J1227.0−4859, which was recently shown to have undergone the reverse transition (Bassa et al. 2014) to a rotation-powered radio pulsar (Roy et al. 2014). The peak 3–79 keV luminosity observed over the 4.75 hr orbital period is 1.2×10^{34} erg s^{-1}. This is significant compared to the rotational energy loss of the pulsar $\dot{E} \approx 4 \times 10^{34}$ erg s^{-1}, considering the low conversion efficiency between spin-down luminosity and X-ray luminosity seen in radio pulsars ($\sim 10^{-3}$ at this luminosity level; Possenti et al. 2002). The absence of orbital modulations in the post-transition light curve is consistent with the X-ray photons being emitted from near the transition region/corona at the inner edge of the accretion disk, possibly dominated by the synchrotron emission as suggested by Papitto et al. (2014b) for XSS J1227.0−4859 (with a very similar power-law spectrum with $\Gamma = 1.7$). We observe that Γ varies only by 0.05 over a factor of seven change in count rate during the flares, which is expected if the optical depth of Comptonization does not change significantly while the source photon population varies. The observed X-ray luminosity of PSR J1023+0038 is in the range of 10^{-7}–10^{-6} $L_{\rm Edd}$, far lower than for atoll sources (which range from 0.01 to 0.5 $L_{\rm Edd}$; e.g., see Ford et al. 2000). The low October X-ray luminosity compared with those of fully accreting neutron stars, along with the nondetection of pulsations, corroborates the absence of material accreting onto the surface of the neutron star.

The lack of a high-energy cutoff in the *NuSTAR* energy range suggests that the highest electron energy in the pulsar wind is $\gtrsim$79 keV. It is likely that the hard X-ray power law and the γ-ray power law cross over at photon energies of 1–10 MeV (red circle in Figure 18). Observations of this energy range would add greatly to our understanding of this enigmatic system.

4.1. Flat-bottomed Dipping

The flat-bottomed dips and flickering observed in the *NuSTAR* and *Swift* observations (Patruno et al. 2014) show the following characteristics that need to be explained by any theoretical interpretation:

1. luminosity variations from $\approx 5 \times 10^{32}$ erg s^{-1} in the low states to a nominal average level of $\approx 6 \times 10^{33}$ erg s^{-1},
2. nonperiodic occurrence, uniformly distributed over orbital phase,
3. nearly flat intensity in the bottom of the dip, with no significant hardness ratio change,
4. ingress and egress timescales between 10 and 60 s,
5. no correlation between dip width and the separation to either the previous or next dip,
6. a log-normal distribution of dip separations, as shown in Figure 15, and
7. a decreasing distribution in dip widths as shown in Figure 16.

This dipping activity is unlike activity observed in other similar systems, namely PSR J1824−2452I (Papitto et al. 2014a) and XSS J1227.0−4859 (de Martino et al. 2013). In the 0.3–10 keV range, *XMM-Newton* observations of PSR J1824−2452I revealed sharp spectral changes as a function of count rate (Ferrigno et al. 2014). The ingress and egress timescales of these dips were about 200 s, the dip widths were up to a few thousand seconds, and the low-state luminosity was $\approx 10^{35}$ erg s^{-1}. The dips were interpreted as abrupt interruptions in accretion of matter onto the surface ("weak" and "strong" propeller regimes; Illarionov & Sunyaev 1975; Ustyugova et al. 2006), reducing the X-ray luminosity and revealing partially obscured thermal emission from the neutron star surface. Linares et al. (2014) reported that archival *Chandra* observations of PSR J1824−2452I in quiescence (defined as $L_X/L_{\rm Edd} < 10^{-4}$) revealed changes between active (L_X(0.3–10 keV) $= 3.9 \times 10^{33}$ erg s^{-1}) and passive (5.6×10^{32} erg s^{-1}) states with no change in the power-law spectral index ($\Gamma \approx 1.5$). The transitions between the two states occurred on timescales of 500 s, and the states lasted for $\sim$10 hr. The authors suggested that the state changes were caused by two different nonthermal emission mechanisms that coincidentally led to the same spectra: the high states being explained by magnetospheric accretion and the low states being attributed to intrabinary shock emission. Similar state change behavior observed in the quiescent LMXB EXO 1745−28 in Terzan 5 was also attributed to variations in accretion rates (Degenaar & Wijnands 2012).

de Martino et al. (2013) observed dips with ingress and egress fast timescales ($\lesssim$10 s) in *XMM-Newton* observations of XSS J1227.0−4859 with dip widths between 200 and 800 s. These dips were observed in the X-ray and near-UV bands but were absent in the ground-based optical observations, suggesting an origin close to the neutron star. The authors attributed dips occurring immediately after flares to sudden accretion onto the neutron star (the flare and the corresponding emptying (the dip) and filling up of the inner regions of the accretion disk. Attempting to interpret the other dips as eclipses (as in the case of LMXB dippers Church & Bałucińska-Church 2004) with dense absorbing material covering a significant fraction of the X-ray source (i.e., the inner disk corona) did not lead to practical results, apart from the lack of periodicity.

Recently, Chakrabarty et al. (2014) reported highly variable flickering from Cen X-4 during recent observations where the

NuSTAR-band luminosity was $\approx 2 \times 10^{32}$ erg s^{-1}. While no dips or eclipses were observed during the observation, variability up to a factor of 20 on timescales of minutes to hours without significant spectral variability was observed. While Cen X-4 has not been directly observed to transition between an LMXB-like to a rotation-powered state, there may be some spectral evidence for such a change in archival data (Chakrabarty et al. 2014). With the caveat of a small sample, it may be that such variability phenomena may be specific to the 10^{32}–10^{33} erg s^{-1} luminosity range, where the systems transition between an LMXB-like and a rotation-powered MSP state.

In our data, the low luminosity (item 1, above), sets them apart from dips occurring due to interrupted accretion onto the neutron star surface. Item 2 makes our observations inconsistent with an association with the binary orbit or a specific radius in the accretion disk. Similarly, the orbital radii corresponding to the 10 s and 100 s timescales are 7800 km and 36,000 km, respectively, far larger than the expected location of hard X-ray source near the light-cylinder radius, $r_{\rm lc} = 81$ km. Item 3 rules out eclipses due to optically thin material, suggesting instead either a change in the source brightness or an eclipse with a dense blob of material. However, the latter hypothesis is unlikely because the dense material would be expected to come to dynamical and thermal equilibrium with its surroundings in timescales of $t_{\rm dynamical} \sim \alpha t_{\rm thermal} \sim (H/R)^2 t_{\rm viscous}$ (see Equation (5.68); Frank et al. 2002), where α is the Shakura–Sunyaev parameterization of disk viscosity (Shakura & Sunyaev 1973) and H and R are the disk height and radius, respectively. The viscous timescale of the inner disk is estimated to be ∼10–100 s (see Patruno et al. 2014), and as $H/R < 1$ for an expected thin disk, we expect these timescales to be very short.

Given the lack of change in the hardness ratio, it is possible that these variations are due to clumpy wind from the pulsar or clumpy accretion flow from the companion star. The viscous timescale of the inner disk (∼10–100 s) is similar to the observed ingress and egress timescales (item 4). A possible explanation may involve the inner disk being pushed back and re-formed on these timescales. The reduced mass transfer rate could diminish the source photon density available for Comptonization without significantly affecting the optical depth and electron temperature (and hence the power-law index Γ). However, it remains to be understood (1) what mechanism would cause the disk to cycle through these states repeatedly, (2) why the ingress and egress timescales are symmetrical, and (3) why there is no correlation between the dip width and separation (item 5). It would be interesting to understand how these changes occur at a fast timescale in PSR J1023+0038 as compared to the long timescale state changes observed in PSR J1824−2452I (Ferrigno et al. 2014) and how they are affected by the accretion state and luminosity of the system. Items 6 and 7 are stated for completeness and need to be considered by a more detailed theoretical explanation but are outside the scope of this discussion.

Another candidate explanation invokes interrupted mass donations from the donor star that propagate through the accretion disk and are observed as dips. However, this scenario is unlikely because (1) it is unlikely for the donor star to vary at 10–100 s timescale unless some seismological/tidal modes are active, in which case, periodicity would be expected; (2) the gaps propagating through the accretion disk would diffuse, leading to long ingress and egress timescales; and (3) the gap propagation from the outer to inner disk would have been observed in different energies at different times, leading to varying hardness ratios.

The well-measured distance of PSR J1023+0038 (1.3 kpc; Deller et al. 2012) is much less than the typical 7–8 kpc distances of other neutron star LMXBs (Jonker & Nelemans 2004), making it a unique and important case study because it allows us to pursue detailed spectral and timing analyses at extremely low luminosity states that are unobservable for most other LMXB sources. Further monitoring of this source is warranted to reveal previously unobserved details of the transitions between LMXBs and MSPs.

We thank the anonymous referee for detailed suggestions and comments. This work was supported under NASA Contract No. NNG08FD60C and made use of data from the *NuSTAR* mission, a project led by the California Institute of Technology, managed by the Jet Propulsion Laboratory, and funded by the National Aeronautics and Space Administration. We thank the *NuSTAR* Operations, Software, and Calibration teams for support with the execution and analysis of these observations. This research made use of the *NuSTAR* Data Analysis Software (NuSTARDAS) jointly developed by the ASI Science Data Center (ASDC, Italy) and the California Institute of Technology (USA). VMK receives support from an NSERC Discovery Grant and Accelerator Supplement, from the Centre de Recherche en Astrophysique du Québec, an R. Howard Webster Foundation Fellowship from the Canadian Institute for Advanced Study, the Canada Research Chairs Program, and the Lorne Trottier Chair in Astrophysics and Cosmology. J.W.T.H. acknowledges funding for this work from ERC starting grant DRAGNET. A.P. acknowledges support from the Netherlands Organization for Scientic Research (NWO) Vidi fellowship.

REFERENCES

Alpar, M. A., Cheng, A. F., Ruderman, M. A., & Shaham, J. 1982, Natur, 300, 728
Archibald, A. M., Kaspi, V. M., Bogdanov, S., et al. 2010, ApJ, 722, 88
Archibald, A. M., Kaspi, V. M., Hessels, J. W. T., et al. 2013, arXiv:1311.5161
Archibald, A. M., Stairs, I. H., Ransom, S. M., et al. 2009, Sci, 324, 1411
Backer, D. C., Kulkarni, S. R., Heiles, C., Davis, M. M., & Goss, W. M. 1982, Natur, 300, 615
Bailes, M., Bates, S. D., Bhalerao, V., et al. 2011, Sci, 333, 1717
Barret, D., & Vaughan, S. 2012, ApJ, 746, 131
Bassa, C. G., Patruno, A., Hessels, J. W. T., et al. 2014, arXiv:1402.0765
Bhattacharya, D., & van den Heuvel, E. P. J. 1991, PhR, 203, 1
Bogdanov, S., Archibald, A. M., Hessels, J. W. T., et al. 2011, ApJ, 742, 97
Bond, H. E., White, R. L., Becker, R. H., & O'Brien, M. S. 2002, PASP, 114, 1359
Burrows, D. N., Hill, J. E., Nousek, J. A., et al. 2005, SSRv, 120, 165
Chakrabarty, D., Tomsick, J. A., Grefenstette, B. W., et al. 2014, arXiv:1403.6751
Church, M. J., & Bałucińska-Church, M. 2004, MNRAS, 348, 955
de Martino, D., Belloni, T., Falanga, M., et al. 2013, A&A, 550, A89
Degenaar, N., & Wijnands, R. 2012, MNRAS, 422, 581
Deller, A. T., Archibald, A. M., Brisken, W. F., et al. 2012, ApJL, 756, L25
Ferrigno, C., Bozzo, E., Papitto, A., et al. 2014, A&A, 567, 77
Ford, E. C., van der Klis, M., Méndez, M., et al. 2000, ApJ, 537, 368
Frank, J., King, A., & Raine, D. J. 2002, Accretion Power in Astrophysics: Third Edition (Cambridge: Cambridge Univ. Press)
Fruchter, A. S., Berman, G., Bower, G., et al. 1990, ApJ, 351, 642
Gonzalez, R. C., & Woods, R. E. 1992, Digital Image Processing (Reading, MA: Addison-Wesley Publishing Company)
Halpern, J. P., Gaidos, E., Sheffield, A., Price-Whelan, A. M., & Bogdanov, S. 2013, ATel, 5514, 1
Harrison, F. A., Craig, W. W., Christensen, F. E., et al. 2013, ApJ, 770, 103
Homer, L., Szkody, P., Chen, B., et al. 2006, AJ, 131, 562
Illarionov, A. F., & Sunyaev, R. A. 1975, A&A, 39, 185
Jonker, P. G., & Nelemans, G. 2004, MNRAS, 354, 355
Kong, A. K. H. 2013, ATel, 5515, 1

Leahy, D. A. 1987, A&A, 180, 275
Leahy, D. A., Darbro, W., Elsner, R. F., et al. 1983, ApJ, 266, 160
Linares, M., Bahramian, A., Heinke, C., et al. 2014, MNRAS, 438, 251
Miyamoto, S., Kimura, K., Kitamoto, S., Dotani, T., & Ebisawa, K. 1991, ApJ, 383, 784
Nolan, P. L., Abdo, A. A., Ackermann, M., et al. 2012, ApJS, 199, 31
Papitto, A., Ferrigno, C., Bozzo, E., & Rea, N. 2014a, in European Physical Journal Web of Conferences, Vol. 64, ed. E. Bozzo et al. (Geneva, Switzerland: EPJ), 1004
Papitto, A., Ferrigno, C., Bozzo, E., et al. 2013, Natur, 501, 517
Papitto, A., Torres, D. F., & Li, J. 2014b, MNRAS, 438, 2105
Patruno, A., Archibald, A. M., Hessels, J. W. T., et al. 2014, ApJL, 781, L3
Patruno, A., & Watts, A. L. 2012, arXiv:1206.2727
Possenti, A., Cerutti, R., Colpi, M., & Mereghetti, S. 2002, A&A, 387, 993
Radhakrishnan, V., & Srinivasan, G. 1982, CSci, 51, 1096
Roberts, M. S. E. 2011, in AIP Conf. Proc. 1357, Radio Pulsars: An Astrophysical Key to Unlock the Secrets of the Universe, ed. M. Burgay, N. D'Amico, P. Esposito, A. Pellizzoni, & A. Possenti (Melville, NY: AIP), 127
Roy, J., Bhattacharyya, B., & Ray, P. S. 2014, ATel, 5890, 1
Shakura, N. I., & Sunyaev, R. A. 1973, A&A, 24, 337
Stappers, B. W., Archibald, A., Bassa, C., et al. 2013, ATel, 5513, 1
Stappers, B. W., Archibald, A. M., Hessels, J. W. T., et al. 2014, ApJ, 790, 39
Takata, J., Li, K. L., Leung, G. C. K., et al. 2014, ApJ, 785, 131
Tam, P. H. T., Hui, C. Y., Huang, R. H. H., et al. 2010, ApJL, 724, L207
Tauris, T. M. 2012, Sci, 335, 561
Thorstensen, J. R., & Armstrong, E. 2005, AJ, 130, 759
Ustyugova, G. V., Koldoba, A. V., Romanova, M. M., & Lovelace, R. V. E. 2006, ApJ, 646, 304
Wang, Z., Archibald, A. M., Thorstensen, J. R., et al. 2009, ApJ, 703, 2017
Wijnands, R., & van der Klis, M. 1998, Natur, 394, 344